

A. DUBIETIS^{1,✉}
A. COUAIRON²
E. KUČINSKAS¹
G. TAMOŠAUSKAS¹
E. GAIŽAUSKAS¹
D. FACCIO³
P. DI TRAPANI³

Measurement and calculation of nonlinear absorption associated with femtosecond filaments in water

¹ Department of Quantum Electronics, Vilnius University, Saulėtekio Avenue 9, Bldg. 3, 10222 Vilnius, Lithuania

² Centre de Physique Théorique, CNRS UMR 7644, École Polytechnique, 91128 Palaiseau Cedex, France

³ Istituto Nazionale di Fisica della Materia (INFM) and Department of Chemical, Physical and Mathematical Sciences, University of Insubria, Via Valleggio 11, 22100 Como, Italy

Received: 20 December 2005 / Revised version: 21 March 2006

Published online: 13 May 2006 • © Springer-Verlag 2006

ABSTRACT We investigate the filamentation dynamics of 200 fs, 527 nm laser pulses in water. By comparing the experimental results with the numerical simulations that use an extended propagation model, the influence of several physical effects, particularly nonlinear losses and free electron plasma generation, is studied. It is shown that a set of relevant numerical values, related to multiphoton absorption, can be extracted with reasonable accuracy.

PACS 42.65.Jx; 42.25.Bs

1 Introduction

Self-focusing of femtosecond light pulses in transparent media gives rise to a variety of physical effects: beam filamentation, conical emission, white-light continuum generation, nonlinear absorption, ionization, space-time transformations, to mention a few, and still remains a hot topic of theoretical and experimental research [1]. Although self-focusing and filamentation of high power optical beams was discovered at the very dawn of the laser era [2], only with the advent of femtosecond lasers has deeper understanding of the underlying physics been made possible [3]. In the last decade, considerable knowledge on self-focusing phenomena has been accumulated, thanks to a revived interest in the topic inspired by the observation of long-range propagation of femtosecond light filaments in air [4].

In this regard, many interesting and even unexpected findings were disclosed, which have a potential impact on complete understanding of the underlying physics and which promote a series of potential applications, as well. Despite very distinct operating conditions, all observations of light filaments in air [4–7], solids [8–11] and liquids [12–15] reported to date reveal the universality of the physical processes involved. The widely accepted filamentation scenario is based upon self-channelled propagation governing the dynamic balance between self-focusing, diffraction and defocusing effects of free electron plasma, created via multiphoton ionization. More recently, an alternative approach based on

the spontaneous transformation of a Gaussian-shaped wave packet into a conical wave, even not accounting for plasma formation at all has been suggested [16]. In this regard, femtosecond filamentation in water was interpreted in terms of dynamic nonlinear X-waves, formed as a consequence of the complex interplay between self-focusing and group velocity dispersion [17]. The full map of spatiotemporal transformations outlined complex dynamics, initially dominated by nonlinear losses, then by self-focusing and pulse splitting, eventually leading to the formation of X-shaped objects surrounded by a structured background [18]. Numerical simulations using a model developed for femtosecond filamentation in liquids, solids and gasses confirmed the experimental observations, and most importantly, have foreseen nonlinear X wave generation for a wide parameter range, regardless of the physical mechanism arresting their collapse [19].

Investigation of spatiotemporal dynamics requires complex experimental arrangements, which must ensure high spatial and temporal resolution (details may be found in [20]). However, a simple experiment providing time-integrated measurements might be useful as well, especially for determining the nonlinear losses, whatever their origin, multiphoton absorption, or ionization. Nonlinear losses (NLL) occur in all transparent materials under operating conditions, which imply strong self-action effects. The simplest manifestation of NLL in condensed media is the multiphoton absorption (MPA), the process involving simultaneous absorption of several photons, when their total energy exceeds that of the materials bandgap. An open question that still needs to be clarified is the role of MPA in filamentation dynamics. Although NLL were predicted to be capable of arresting the collapse driven by Kerr-induced self-focusing [21–24], they have been rarely considered as a relevant mechanism that might contribute to reshaping the wave packet. Only recently, NLL had been shown to dramatically modify the spatial profile of the beam in the presence of strong self-focusing effects in water [16], polymers [25] and glass [26], while in the latter case NLL was indicated for serving as an intensity limiting mechanism. The major problem related to the reliable reproduction of the experimental results by numerical simulations is the lack of knowledge of MPA coefficients, which are not known with reasonable precision from theory, and cannot be directly measured in experiments by simple means. The major difficulty comes from a complex interplay between nonlinear

✉ Fax: +370 52 366006, E-mail: audrius.dubietis@ff.vu.lt

spatiotemporal effects that cannot be separated in real experimental settings (see [25] for a comprehensive evaluation of the problem).

The aim of this paper is that of providing a comprehensive insight into the relevant physical processes that accompany self-focusing and filamentation of ultrashort light pulses in water. In the experiment we have recorded three relevant time-integrated quantities, namely the beam width, peak fluence and energy transmission, which do not require complex experimental arrangement, are easily accessible in a simple setup and however, carry important information on the physical processes involved. Using a recently developed extended numerical propagation model, we compared the computed dynamics of these three quantities with their measured counterparts, with the best fit between numerics and experiment allowing the estimation of the MPA coefficient in water.

2 The model

We performed numerical simulations using the model developed for the propagation of an intense pulse in transparent dispersive nonlinear media [6–8, 16, 17, 27–30].

We model the linearly polarized beam (along \mathbf{e}_x) with cylindrical symmetry around the propagation axis z by the envelope \mathcal{E} of the electric field \mathbf{E} , written as $\mathbf{E} = \text{Re}[\mathcal{E} \exp(ik_0 z - i\omega_0 t)]\mathbf{e}_x$, where $k_0 = n_0 \omega_0 / c$ and $\omega_0 \equiv 2\pi/\lambda_0$ are the wavenumber and frequency of the carrier wave and n_0 denotes the refraction index of water at ω_0 . The laser wavelength is $\lambda_0 = 527$ nm throughout this paper. The input pulses are modelled by Gaussians with energy E_{in} and a temporal half width $t_p \sim 170$ fs (full width half maximum (FWHM) duration $\tau_{\text{FWHM}} = 200$ fs):

$$\mathcal{E}(r, t, 0) = \mathcal{E}_0 \exp\left(-\frac{r^2}{w_0^2} - \frac{t^2}{t_p^2}\right). \quad (1)$$

The input power is computed from the energy and pulse duration $P_{\text{in}} = E_{\text{in}}/t_p \sqrt{\pi/2}$ and the input intensity is computed from the input power and the transverse waist w_0 of the beam $\mathcal{E}_0^2 = 2P_{\text{in}}/\pi w_0^2$. The scalar envelope $\mathcal{E}(r, t, z)$ evolves along the propagation axis z according to the nonlinear envelope equation [31], expressed in the frequency domain:

$$\hat{U} \frac{\partial \hat{\mathcal{E}}}{\partial z} = i \left[\frac{\nabla_{\perp}^2}{2k} + \frac{k_0}{2} \left(\frac{n^2 \omega^2}{k_0^2 c^2} - \hat{U}^2 \right) \right] \hat{\mathcal{E}} + \text{TF}\{N(\mathcal{E})\}, \quad (2)$$

where $\hat{\mathcal{E}}(r, \omega, z) = \text{TF}\{\mathcal{E}(r, t, z)\}$, $\hat{U}(\omega) \equiv 1 + (\omega - \omega_0)/k_0 v_g$, $v_g \equiv \partial\omega/\partial k|_{\omega_0}$ denotes the group velocity and $\text{TF}\{N(\mathcal{E})\}$ denotes the time-Fourier transform of the nonlinear terms. Equation (2) accounts for diffraction in the transverse plane, space-time focusing (see [31, 32]), and group velocity dispersion with high-order terms exactly computed by means of a Sellmeier dispersion relation for the refraction index $n(\omega)$ of water [33]. The origin of the second term on the right hand side of (2) may be understood by a small $\omega - \omega_0$ expansion of the quantity

$$\hat{U}^{-1} \left(\frac{n^2 \omega^2}{k_0^2 c^2} - \hat{U}^2 \right) \sim \frac{k''}{k_0} (\omega - \omega_0)^2 + \frac{k'''}{3k_0} (\omega - \omega_0)^3 + \dots \quad (3)$$

leading to the second and third order dispersive coefficients $k'' \equiv \partial^2 k / \partial \omega^2|_{\omega_0}$ and $k''' \equiv \partial^3 k / \partial \omega^3|_{\omega_0}$, where $k = n(\omega)\omega/c$.

Equation (2) can be written in the time domain by using the retarded time $t \equiv t_{\text{lab}} - z/v_g$ and by neglecting the high-order dispersive terms:

$$\frac{\partial \mathcal{E}}{\partial z} = \frac{i}{2k_0} U^{-1} \nabla_{\perp}^2 \mathcal{E} - i \frac{k''}{2} \frac{\partial^2 \mathcal{E}}{\partial t^2} + \frac{k'''}{6} \frac{\partial^3 \mathcal{E}}{\partial t^3} + U^{-1} N(\mathcal{E}), \quad (4)$$

where $U \equiv (1 + \frac{i}{k_0 v_g} \frac{\partial}{\partial t})$. For the numerical simulations, we have used model (2) with the full dispersion relation given by (12) in [33] that gives the dispersive coefficients values $k'' = 560 \text{ fs}^2/\text{cm}$, $k''' = 180 \text{ fs}^3/\text{cm}$, in agreement with the measurements [33].

The nonlinear terms $N(\mathcal{E})$ include the optical Kerr effect with possible optical shock terms (self-steepening), plasma absorption, plasma defocusing and nonlinear losses:

$$N(\mathcal{E}) = ik_0 n_2 T^2 |\mathcal{E}|^2 \mathcal{E} - \frac{\sigma}{2} (1 + i\omega_0 \tau_c) \mathcal{Q} \mathcal{E} - T \frac{\beta_K}{2} \left(1 - \frac{\mathcal{Q}}{\mathcal{Q}_{\text{be}}}\right) |\mathcal{E}|^{2K-2} \mathcal{E}. \quad (5)$$

Here, the operator $T \equiv 1 + \frac{i}{\omega_0} \frac{\partial}{\partial t}$ in front of the Kerr term is responsible for the self-steepening of the pulse (the so-called shock terms) [32, 34, 35]. The quantity $n_2 = 2.7 \times 10^{-16} \text{ cm}^2/\text{W}$ denotes the coefficient of the nonlinear index of water, leading to the critical power for self-focusing $P_{\text{cr}} = 1.2 \text{ MW}$. The generation of an electron plasma of density \mathcal{Q} via multiphoton ionization is described below. When they are taken into account, nonlinear losses correspond to multiphoton absorption, i.e. to the fraction of the pulse energy needed for ionization. In the following, some results will be presented also in the case where plasma generation is not accounted for. In this case, NLL are assumed to describe excitation of water molecules.

The evolution equation for the electron density \mathcal{Q} reads

$$\frac{\partial \mathcal{Q}}{\partial t} = \sigma_K |\mathcal{E}|^{2K} (\mathcal{Q}_{\text{be}} - \mathcal{Q}) + \frac{\sigma}{U_i} \mathcal{Q} |\mathcal{E}|^2. \quad (6)$$

The first term on the right hand side of (6) describes free electron generation via multiphoton ionization (MPI). The second term in (6) accounts for avalanche ionization. The quantities $\mathcal{Q}_{\text{be}} = 6.7 \times 10^{22} \text{ cm}^{-3}$ denotes the density of bound electrons [36], $U_i = 6.5 \text{ eV}$ denotes the ionization potential of water, and $K \equiv \lfloor \frac{U_i}{\hbar \omega_0} + 1 \rfloor = 3$ (where $\lfloor \cdot \rfloor$ denotes the integer part) is the number of photons necessary to liberate an electron. When multiphoton ionization is taken into account, the coefficient for multiphoton ionization is linked to the multiphoton absorption cross-section: $\beta_K = \sigma_K \times K \hbar \omega_0 \mathcal{Q}_{\text{be}}$.

For plasma absorption, the cross section for inverse bremsstrahlung follows the Drude model [37] and reads

$$\sigma = \frac{k_0 e^2}{n_0^2 \omega_0^2 \epsilon_0 m_e} \times \frac{\omega_0 \tau_c}{1 + \omega_0^2 \tau_c^2}, \quad (7)$$

where the momentum transfer collision time $\tau_c = 3 \text{ fs}$. Since $\tau_c \gg \omega_0^{-1}$, avalanche ionization can often be neglected, at least until a non-negligible number of electrons are produced in the leading part of the laser pulse via multiphoton ionization.

In this case, plasma absorption is neglected as well and the plasma defocusing term in (5) is written as:

$$-i \frac{\sigma \omega_0 \tau_c \mathcal{Q} \mathcal{E}}{2} \sim -i \frac{k_0 \mathcal{Q}}{2 n_0^2 \mathcal{Q}_c} \mathcal{E}, \quad (8)$$

where $\mathcal{Q}_c \equiv \epsilon_0 m_e \omega_0^2 / e^2$ denotes the critical plasma density above which the plasma becomes opaque. As will be seen from the results, however, plasma absorption as computed from this model can induce half the total amount of energy losses measured in experiments, and the fraction of electron density directly originating from avalanche can be as large as that originating from MPI.

The energy was computed by two independent methods: (i) the energy is directly calculated by a 3-dimensional integration of the intensity distribution within the computational box, and (ii) we numerically simulated the conservation equation for energy. Since multiphoton absorption is a high order nonlinear term, only the intense part of the wave gives a significant contribution to the losses. The second method is therefore not sensitive to the effects of box size and boundary conditions. We checked that both methods give identical results, which ensures that the simulated losses cannot be caused by fields leaving the computational box.

3 Experimental

In the experiment, spatially filtered and collimated 527 nm, 200 fs laser pulses (provided by a SHG-compressed, CPA Nd:glass laser TWINKLE, Light Conversion, operated at 33 Hz repetition rate) were focused on the input face of a water cell by means of a $f = +500$ mm lens. This resulted in a 90 μm FWHM diameter spot. Unlike in experiments performed under tight focusing conditions [10–12, 14, 28], loose focusing prevented a competition between filamentation and optical breakdown. The water cell was made by 1 mm thick fused silica windows and shaped as a syringe, which allowed continuous tuning of the sample length in the range $z = 5$ –50 mm. The output beam was monitored by imaging the exit facet of the cell onto a CCD camera (COHU, with a frame grabber from Spiricon, supporting a 10-bit dynamic range) by means of a $f = +50$ mm achromatic objective, with $8\times$ magnification. The energy was measured by means of a calibrated silica photodiode (Hamamatsu, with 33 mm² effective area), with the spectral response function taken into account.

We have recorded time-integrated transverse beam profile dynamics along with energy transmission measurements versus the propagation distance using a 2–3 mm step. The input energy of 2 μJ was chosen as a representative value, that ensured formation of a single filament after ~ 1 cm of propagation in water and exhibited more or less typical propagation dynamics. Few examples of measured fluence profiles, recorded at $z = 5, 11, 15$ and 35 mm are shown in Fig. 1. Three relevant quantities from this measurement were evaluated, namely the peak fluence, the transmitted energy and FWHM radius of the beam. For what which concerns the latter quantity, we found that the notion of FWHM beam radius is relevant for characterizing the beam since no dip appeared in the core of the measured (or computed) fluence profiles.

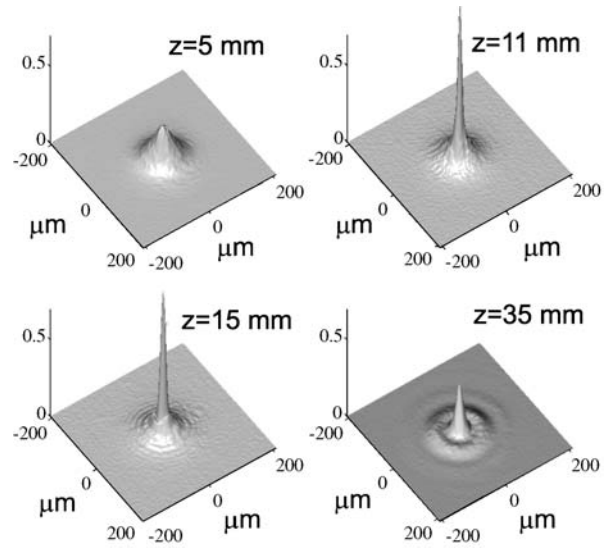


FIGURE 1 Experimentally measured normalized fluence profiles in water of loosely focused 90 μm FWHM, 200 fs, 2 μJ Gaussian wave-packet with a central wavelength of 527 nm

In addition, it gives an immediate picture of the smooth focusing dynamics obtained in our experimental conditions. For direct comparison, this experimental data set is added to all the Figs. 4–7 that represent the results of numerical simulations.

In brief, the experimental data shows that in the first few millimeters of propagation, a gradual decrease of the initial Gaussian beam size is observed due to self-focusing. No NLL occur in this stage, since the intensity is still too low. Once a certain intensity level is reached, NLL turns on, immediately resulting in a rapid transformation of the beam shape. Beyond the nonlinear focus, a single filament of radius less than 10 microns is formed, however NLL become considerably smaller than in the transient stage. This observation could be explained by the fact that only a small portion of the overall energy is stored in the central core (less than 10%), whereas the major part spreads in the low-intensity periphery that serves as an energy reservoir (see [16]). Therefore the overall losses become small, and a sharp central spike (filament) propagates almost unaffected, with a smooth increase of dimensions for $z > 4$ cm. The normalized peak fluence exhibits an abrupt increase during the self-focusing stage followed by a smooth decay beyond the nonlinear focus.

In the following sections, the results of the numerical experiments are compared with those of the laboratory experiments in order to evaluate the relevant parameters involved in the propagation dynamics.

4 Numerical simulations of the filament dynamics

In our model, water is treated as an amorphous semiconductor [36] with a bandgap of 6.5 eV between the valence and the conduction band, allowing the calculation of multiphoton absorption cross sections from Keldysh's model [38]. In addition to the laser wavelength and the bandgap, Keldysh's model needs the estimation of the effective electron–hole mass ratio; a non parabolic band shape is also assumed, which can affect the ionization rates. Figure 2

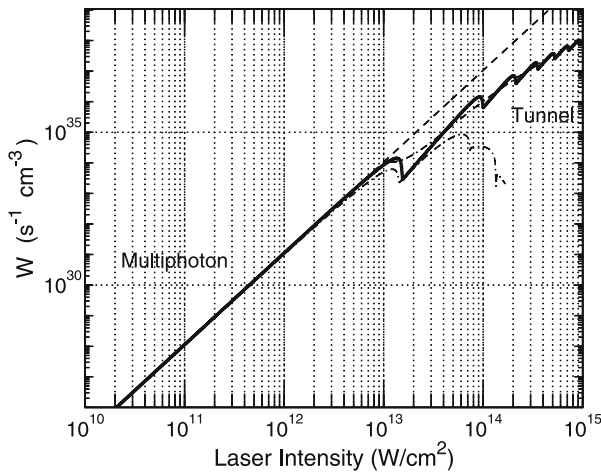


FIGURE 2 Calculated ionization rate W (solid line) for water from Keldysh's theory in the multiphoton and tunnel limits (dash-dotted curves). Asymptotic law $W = \sigma_K I^K \rho_{be}$ is shown by a dashed line

shows the transition rate from the $1b1$ molecular orbital to an exciton band for water at 527 nm, computed from Keldysh's model with the exciton reduced mass ratio $m^*/m_e = 0.5$ and the bandgap $U_i = 6.5$ eV. The multiphoton and tunnel limits (low and high intensity, respectively) are shown by dash-dotted curves and the dashed line indicates the asymptotic law $W = \sigma_K I^K \rho_{be}$. In the present case, Keldysh's model gives $\beta_K = 1.2 \times 10^{-23} \text{ cm}^3/\text{W}^2$ and $\sigma_K = 1.5 \times 10^{-28} \text{ s}^{-1} \text{ cm}^6/\text{W}^3$ for $K = 3$ at 527 nm. This asymptotic rate coincides with the Keldysh transition rate for intensities below $10^{13} \text{ W}/\text{cm}^2$, which is the regime of our simulations thus justifying that working with the power law $W = \sigma_K I^K \rho_{be}$ does not lead to overestimation of the transition rates. However, it is not obvious a priori whether the Keldysh formulation [38, 41, 42] applies for water. Indeed, as it will be shown below, our simulations performed with the above-mentioned material parameters have led to a strong overestimation of the NLL. Therefore, in what follows we find it useful to keep the NLL (K and β_K) and the collision time τ_c as free parameters, and to discuss their impact separately in the framework of three models of increasing complexity for what concerns the number of contributions accounted for in the description of the nonlinear term (5). As will be seen below, in order to reproduce the measured transmission correctly, we should use multiphoton absorption cross-sections two orders of magnitude lower than those computed from Keldysh's model.

To begin with, we first ascertained that numerically simulated fluence profiles (an intense central core surrounded by an evolving ring structure, see Fig. 3) of the self-focusing beam are in good agreement with those measured experimentally (Fig. 1). Moreover, the qualitative agreement was found to be persistent in a broad range of numerical parameters. It has to be noted, however, that the change in the relevant simulation parameters (K , β_K and τ_c) as will be discussed below, more visibly modifies the peak fluence, and the location at which these rings appear.

We first focus attention on the influence of K and β_K , while neglecting the role of τ_c . Figures 4 and 5 show the computed transmission, beam width and fluence as functions of the propagation distance. The left columns refer to the

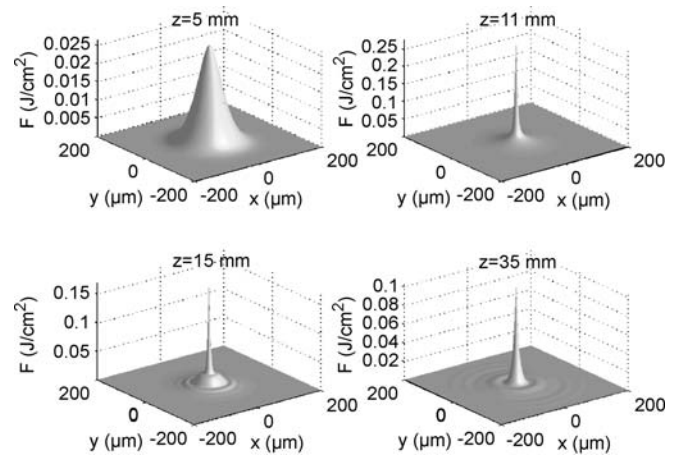


FIGURE 3 Fluence profiles obtained by numerical simulation with input parameters as in experiment using full model with $\beta_K = 8 \times 10^{-25} \text{ cm}^3/\text{W}^2$, avalanche and plasma absorption included with $\tau_c = 3$ fs

model without plasma ($\varrho = 0$ in (5); the model will be referred to as “NLL”), while the right columns refer to the model with plasma generation by MPI (no avalanche in (6)) and associated plasma defocusing term in (5), as given by (8), which is independent of τ_c ; the model will be referred to as “NLL+Plasma”. Figure 4 shows results for $K = 3$ and Fig. 5 for $K = 4$, each figure corresponding to a set of three β_K values given in the captions and chosen around that obtained from Keldysh's model. As a first general comment, we note that, apart from specific details, the results are qualitatively and quantitatively comparable for $K = 3$ and $K = 4$. Second, we note that with these parameter setting, the computed NLL are always larger than those measured experimentally. By decreasing the value of β_K , the transmission increases, but at the same time, the beam width decreases and the fluence exhibits several maxima corresponding to successive refocusing cycles as in the spatial replenishment model [6]. This feature is visible for both models with NLL only, and with ‘NLL+Plasma’ with replenishment oscillations more pronounced in the first case despite the absence of the plasma-defocusing stage occurring in the spatial replenishment model. Note that the peaks in fluence occur in concomitance with minimum values of beam width, which might lead to a smoothing effect in the experiment owing to technical limitation in transverse resolution. A beam width and fluence dynamics comparable to those found in the experiments are obtained for β_K values between 2×10^{-24} and $2 \times 10^{-23} \text{ cm}^3/\text{W}^2$ with $K = 3$, however the NLL are still twice as large as those measured, so this β_K value clearly needs to be decreased. In addition, plasma absorption is not accounted for. Had we taken plasma absorption into account, the overall losses would have been even larger.

We now discuss the influence of τ_c . Figure 6 shows the transmission, beam width and fluence computed with the full model (5) including plasma absorption and avalanche as functions of the propagation distance. The fixed lowest value $\beta_K = 2 \times 10^{-24} \text{ cm}^3/\text{W}^2$ was used as well as a set of three different collision times from 1 to 10 fs, which is a reasonable range in view of the recent determination from measurements of the collision time in fused silica of about 1 fs [43]. In this range, the transmission computed in water is still too small even if it

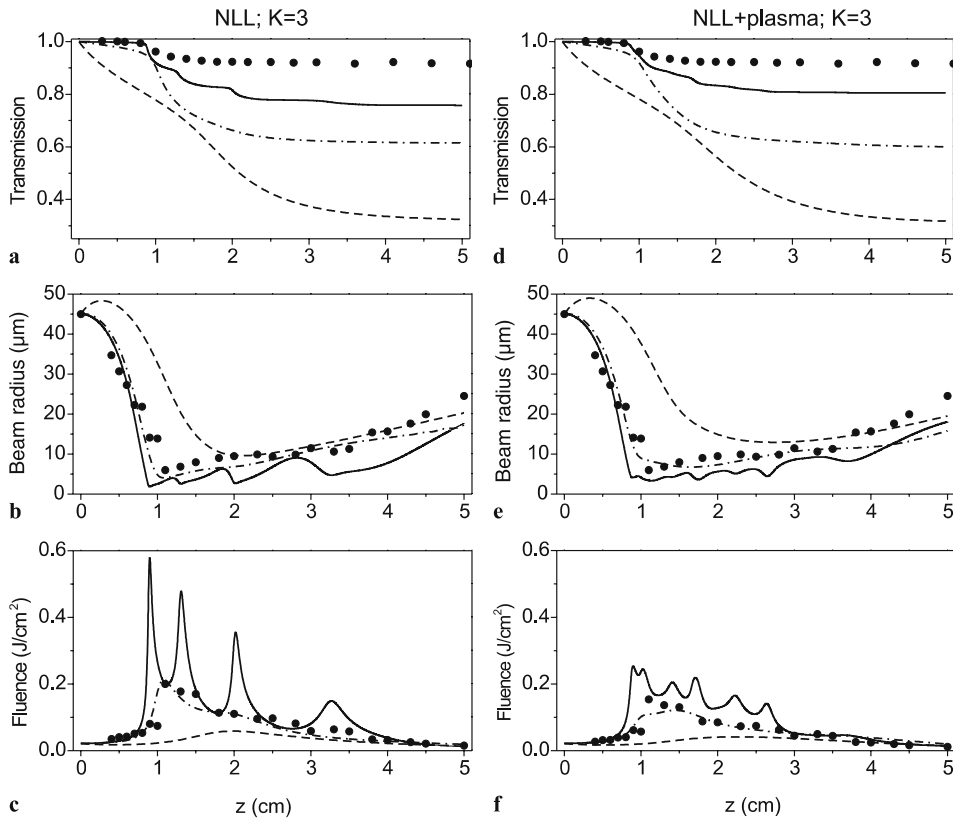


FIGURE 4 Numerical simulations of transmission, beam radius, and fluence evolution with $K = 3$ for different models with NLL (a–c) and plasma defocusing+NLL (d–f). Plasma absorption and avalanche are neglected here. The input pulse duration is 200 fs, pulse energy is 2 μJ , and the experimental data are shown by dots. Three different cross sections have been used: $\beta_K = 2 \times 10^{-22} \text{ cm}^3/\text{W}^2$ (dashed curves); $\beta_K = 2 \times 10^{-23} \text{ cm}^3/\text{W}^2$ (dash-dotted curves); $\beta_K = 2 \times 10^{-24} \text{ cm}^3/\text{W}^2$ (continuous curves)

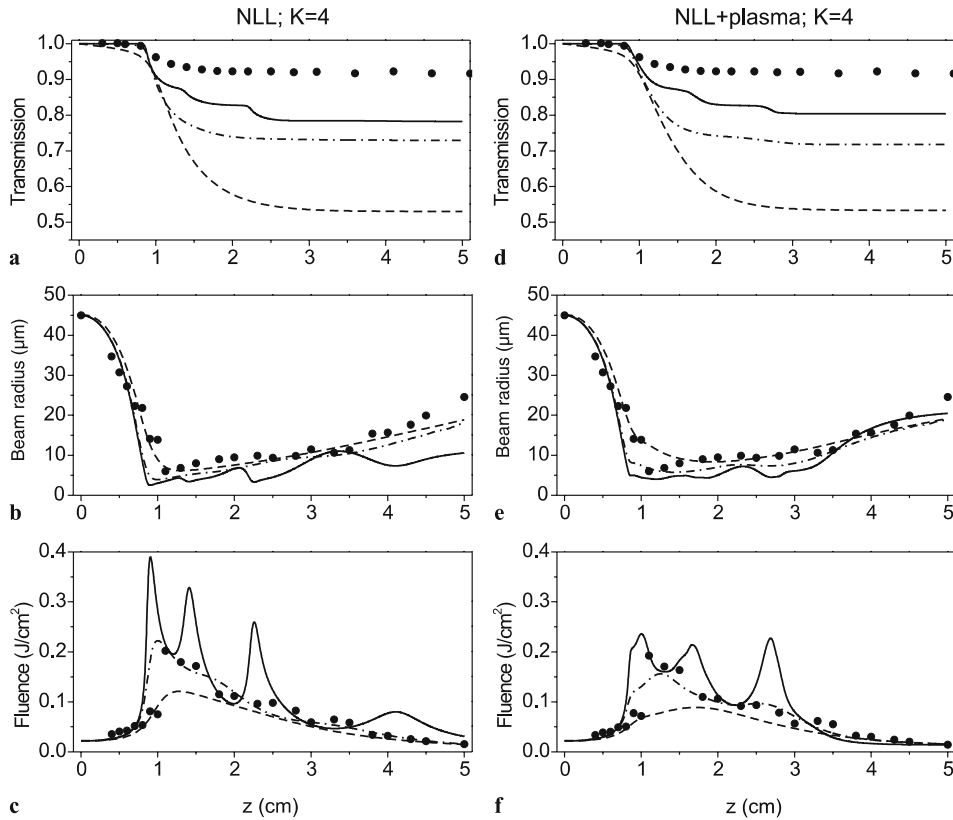


FIGURE 5 Same as in Fig. 4 with $K = 4$ and the coefficients $\beta_K = 2 \times 10^{-34} \text{ cm}^5/\text{W}^3$ (dashed curves); $\beta_K = 2 \times 10^{-35} \text{ cm}^5/\text{W}^3$ (dash-dotted curves); $\beta_K = 2 \times 10^{-36} \text{ cm}^5/\text{W}^3$ (continuous curves)

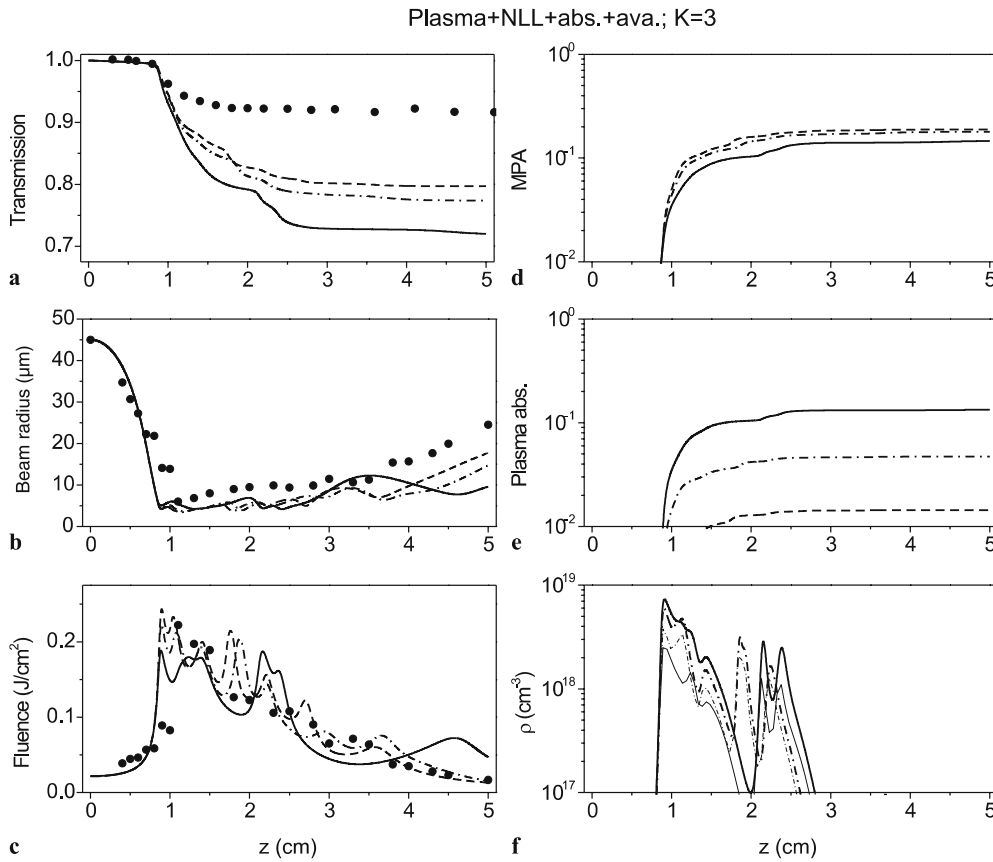


FIGURE 6 First column: Same as in Fig. 4 with $K = 3$ and $\beta_K = 2 \times 10^{-24} \text{ cm}^3/\text{W}^2$ for the full model (5) including plasma absorption and avalanche. Second column: (d) fraction of energy lost by MPA, (e) fraction of energy lost by plasma absorption, (f) electron density with MPI only (thin curves) and MPI+avalanche (bold curves). Three values of the collision time have been used: $\tau_c = 10 \text{ fs}$ (dashed curves); $\tau_c = 3 \text{ fs}$ (dash-dotted curves); $\tau_c = 1 \text{ fs}$ (continuous curves) in all subfigures except in (f) where only the curves for 1 and 3 fs are shown

is increasing when τ_c is increased. In addition, the various fluence peaks are distributed differently when τ_c varies, but still indicate refocusing cycles that do not seem to appear in the experiments (at least for a chosen z step in the measurement).

A logical approach is now to simultaneously decrease the value of β_K sufficiently, and increase the rate of plasma absorption (by decreasing τ_c), so as to reach the amount of total losses found experimentally. Note, however, that it cannot be expected that this provides a smoothing mechanism completely removing the refocusing cycles, because the results for the model “NLL” with no plasma defocusing in Figs. 4 and 5 have shown that these cycles were already present when β_K is decreased so as to fit the experimental transmission. Figure 6d shows the fraction of energy lost by multiphoton absorption and Fig. 6e shows the losses due to plasma absorption. MPA remains nearly the same for the three different values of τ_c as expected. Since β_K is the same for the three curves, the slight variation in MPA is only due to the change in the propagation dynamics related to the contribution of plasma defocusing. The losses by MPA amounts to 15 to 20% of the total energy. Figure 6e shows that part of the energy losses due to plasma absorption varies from a few (for $\tau_c = 10 \text{ fs}$) to 12% (for $\tau_c = 1 \text{ fs}$). Therefore, it is expected that the energy losses due to plasma absorption can be as large as those due to MPA when collision times are comparable to the values measured in other condensed media [43]. Figure 6f shows the electron density obtained for two values $\tau_c = 1 \text{ fs}$ in continuous curves and $\tau_c = 3 \text{ fs}$ in dash-dotted curves. While the maximum electron density is not extremely large for a condensed medium (between 10^{18} and 10^{19} cm^{-3}), the fraction of electrons gen-

erated by avalanche increases and becomes even larger, by a factor of three, than that generated by MPI only when the collision time is decreased down to $\tau_c = 1 \text{ fs}$.

In Fig. 7 we present the results obtained by simultaneously decreasing the value of β_K and increasing the value of τ_c in order to obtain the optimum matching between measured and calculated NLL. The best fit was obtained for $\beta_3 = 1 \times 10^{25} \text{ cm}^3/\text{W}^2$ and $\tau_c = 3 \text{ fs}$. With these parameters, however, the calculated diameters appear to be approximately twice as small as their measured counterparts, and the peak fluence shows fairly fast oscillations in z , which were never detected in our measurements. These oscillations could be partially washed out in the experiment owing to coarse sampling in z and to some smoothing caused by limited transverse resolution in the imaging system (note that the peaks in fluence occur in connection with minimum beam width). On the other hand, the outlined residual discrepancy between measurements and calculation could be also attributed to the presence of physical effects not properly accounted for by our model. Figure 7d and 7e finally show the computed losses due to MPA and plasma absorption. The results indicate that the two contributions are comparable, for the case under examination. Note also that the electron density generated by avalanche is comparable to that generated by MPI, as shown in Fig. 7f.

Figure 8 shows a comparison between measurements and numerical simulations performed for the full model with the MPA cross section $\beta_3 = 1 \times 10^{25} \text{ cm}^3/\text{W}^2$ and $\tau_c = 3 \text{ fs}$. For the three energies of 1, 1.5 and $2 \mu\text{J}$, the bold curves indicating the simulations are nearly superimposed on the data points

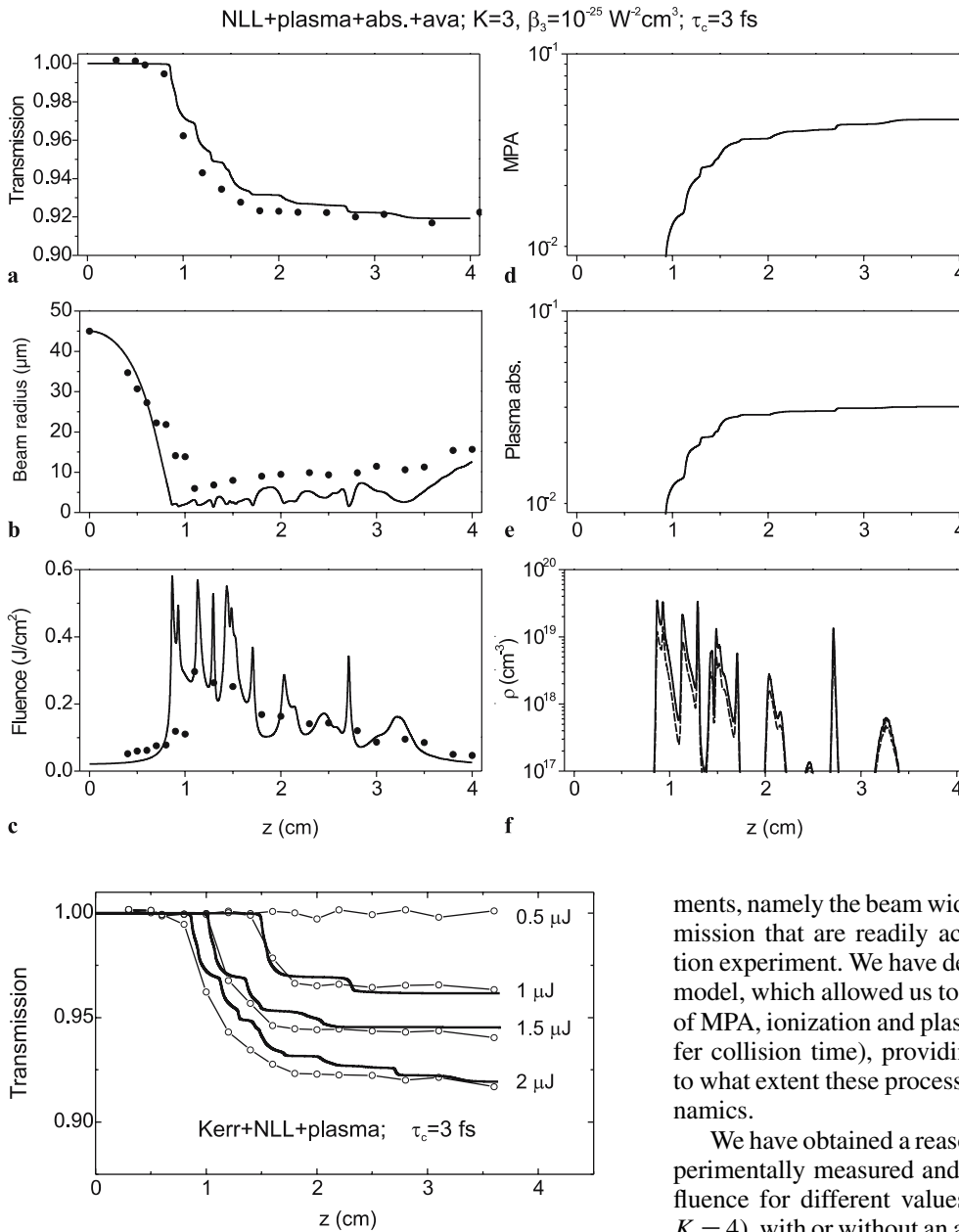


FIGURE 8 Best fit between the computed and the measured transmissions as a function of the propagation distance. The *open circles* are the measurements for 0.5 μJ , 1 μJ , 1.5 μJ and 2 μJ , and the *bold curves* indicate the simulations with the full model with $\beta_3 = 1 \times 10^{-25} \text{ cm}^3/\text{W}^2$ and $\tau_c = 3 \text{ fs}$

showing the transmission data for energies from 0.5 to 2.5 μJ . In these cases, the fraction of energy losses due to plasma absorption was found to represent 50% of the total energy losses. The electron density generated by MPI is comparable to that generated by avalanche. The good agreement obtained in this energy range indicates that the determined MPA cross section is a reasonable value to model nonlinear losses in water.

5 Conclusions

In summary, we have presented numerical and experimental investigation of self-focusing dynamics and filamentation in water by comparing time-integrated measure-

FIGURE 7 Numerical simulations (curves) with full model with $\beta_3 = 1 \times 10^{-25} \text{ cm}^3/\text{W}^2$ estimated from the best fit of the measured transmission (*open circles*). The subfigures show transmission (a), beam radius (b), fluence evolution (c), MPA (d), plasma absorption (e) and free electron density (f) with MPI only (*thin curves*) and MPI+avalanche (*bold curves*)

ments, namely the beam width, peak fluence and energy transmission that are readily accessible from a simple propagation experiment. We have developed an extended propagation model, which allowed us to investigate in great detail the role of MPA, ionization and plasma absorption (momentum transfer collision time), providing a detailed picture of how and to what extent these processes influence the filamentation dynamics.

We have obtained a reasonable agreement between the experimentally measured and calculated beam width and peak fluence for different values of the MPA order ($K = 3$ and $K = 4$), with or without an account for plasma generation (for a simplified model). The best fit yielded an MPA coefficient $\beta_3 = 2 \times 10^{-23} \text{ cm}^3/\text{W}^2$, which is very close to that calculated from the Keldysh model ($\beta_3 = 1.2 \times 10^{-23} \text{ cm}^3/\text{W}^2$). However, in this case significant differences between measured and calculated nonlinear losses are observed; as a general rule, the calculated NLL value always tends to be larger than that experimentally measured. A better agreement for NLL was achieved by decreasing the MPA coefficient (by an order of magnitude) and increasing the collision time (from 1 fs to 3 fs) along with the inclusion of plasma absorption and avalanche ionization, which nevertheless still yields a factor of two in disagreement with measured and calculated NLL values. Finally, the full model accounting for plasma generation, avalanche ionization and plasma absorption is able to reproduce NLL within a reasonable range of input energies with $\tau_c = 3 \text{ fs}$ and $\beta_3 = 1 \times 10^{-25} \text{ cm}^3/\text{W}^2$. However, a factor of two of mismatch in the beam diameter is obtained in the latter case.

In summary, an overall good agreement between measurements and calculations was found in a fairly broad range of parameters. However, difficulty was encountered in perfectly matching both the nonlinear losses and the beam diameter evolution (or the peak fluence). Even if technical limitations in our experimental apparatus could have played some role (in smoothing the fluence dynamics and increasing the diameters owing to finite transverse resolution, and leading to an underestimation of the nonlinear losses, due to a possible presence of a pre-and post pulse temporal energy background in our pump source), the outlined discrepancies might indicate a limitation of the adopted model, and hence the need for including additional physical effects as, e.g. a delayed contribution in the optical Kerr effect [44].

REFERENCES

- 1 A.L. Gaeta, *Science* **301**, 54 (2003)
- 2 R.Y. Chiao, E. Garmire, C.H. Townes, *Phys. Rev. Lett.* **13**, 479 (1964)
- 3 D. Strickland, P.B. Corkum, *J. Opt. Soc. Am. B* **11**, 492 (1994)
- 4 A. Braun, G. Korn, X. Liu, D. Du, J. Squier, G. Mourou, *Opt. Lett.* **20**, 73 (1995)
- 5 O.G. Kosareva, V.P. Kandidov, A. Brodeur, C.Y. Chien, S.L. Chin, *Opt. Lett.* **22**, 1332 (1997)
- 6 M. Mlejnek, E.M. Wright, J.V. Moloney, *Opt. Lett.* **23**, 382 (1998)
- 7 A. Couairon, S. Tzortzakis, L. Bergé, M. Franco, B. Prade, A. Mysyrowicz, *J. Opt. Soc. Am. B* **19**, 1117 (2002)
- 8 S. Tzortzakis, M. Franco, B. Prade, A. Mysyrowicz, A. Couairon, L. Bergé, *Phys. Rev. Lett.* **87**, 213902 (2001)
- 9 Z. Wu, H. Jiang, L. Luo, H. Guo, H. Yang, Q. Gong, *Opt. Lett.* **27**, 448 (2002)
- 10 N.T. Nguyen, A. Saliminia, W. Liu, S.L. Chin, R. Valée, *Opt. Lett.* **28**, 1591 (2003)
- 11 A. Couairon, L. Sudrie, M. Franco, B. Prade, A. Mysyrowicz, *Phys. Rev. B* **71**, 125435 (2005)
- 12 Q. Feng, J.V. Moloney, A.C. Newell, E.M. Wright, *Opt. Lett.* **20**, 1958 (1995)
- 13 A. Brodeur, F.A. Ilkov, S.L. Chin, *Opt. Commun.* **129**, 193 (1996)
- 14 W. Liu, O.G. Kosareva, I.S. Golubtsov, A. Iwasaki, A. Becker, V.P. Kandidov, *Appl. Phys. B* **76**, 215 (2003)
- 15 A. Dubietis, G. Tamošauskas, I. Diomin, A. Varanavičius, *Opt. Lett.* **28**, 1269 (2003)
- 16 A. Dubietis, E. Gaižauskas, G. Tamošauskas, P. Di Trapani, *Phys. Rev. Lett.* **92**, 253903 (2004)
- 17 M. Kolesik, E.M. Wright, J.V. Moloney, *Phys. Rev. Lett.* **92**, 253901 (2004)
- 18 D. Faccio, A. Matijošius, A. Dubietis, R. Piskarskas, A. Varanavičius, E. Gaižauskas, A. Piskarskas, A. Couairon, P. Di Trapani, *Phys. Rev. E* **72**, 037601 (2005)
- 19 A. Couairon, E. Gaižauskas, D. Faccio, A. Dubietis, P. Di Trapani, *Phys. Rev. E* **73**, 016608 (2006)
- 20 J. Trull, O. Jedrkiewicz, P. Di Trapani, A. Matijošius, A. Varanavičius, G. Valiulis, R. Danielius, E. Kučinskas, A. Piskarskas, *Phys. Rev. E* **69**, 026607 (2004)
- 21 S.N. Vlasov, L.V. Piskunova, V.I. Talanov, *Sov. Phys. JETP* **68**, 1125 (1989)
- 22 N.E. Kosmatov, V.F. Shvets, V.E. Zakharov, *Physica D* **52**, 16 (1991)
- 23 S. Dyachenko, A.C. Newell, A. Pushkarev, V.E. Zakharov, *Physica D* **57**, 96 (1992)
- 24 B.J. LeMesurier, *Physica D* **138**, 334 (2000)
- 25 S. Polyakov, F. Yoshino, G.I. Stegeman, *J. Opt. Soc. Am. B* **18**, 1891 (2001)
- 26 D.M. Rayner, A. Naumov, P.B. Corkum, *Opt. Express* **13**, 3208 (2005)
- 27 Q. Feng, J.V. Moloney, A.C. Newell, E.M. Wright, K. Cook, P.K. Kennedy, D.X. Hammer, B.A. Rockwell, C.R. Thompson, *IEEE J. Quantum Electron.* **QE-33**, 127 (1997)
- 28 L. Sudrie, A. Couairon, M. Franco, B. Lamouroux, B. Prade, S. Tzortzakis, A. Mysyrowicz, *Phys. Rev. Lett.* **89**, 186601 (2002)
- 29 A. Couairon, G. Méchain, S. Tzortzakis, M. Franco, B. Lamouroux, B. Prade, A. Mysyrowicz, *Opt. Commun.* **225**, 177 (2003)
- 30 M. Kolesik, J.V. Moloney, G. Katona, E.M. Wright, *Appl. Phys. B* **77**, 185 (2003)
- 31 T. Brabec, F. Krausz, *Phys. Rev. Lett.* **78**, 3282 (1997)
- 32 A.L. Gaeta, *Phys. Rev. Lett.* **84**, 3582 (2000)
- 33 A.G. Van Engen, S.A. Diddams, T.S. Clement, *Appl. Opt.* **37**, 5679 (1998)
- 34 A.A. Zozulya, S.A. Diddams, T.S. Clement, *Phys. Rev. A* **58**, 3303 (1998)
- 35 A.A. Zozulya, S.A. Diddams, A.G. Van Engen, T.S. Clement, *Phys. Rev. Lett.* **82**, 1430 (1999)
- 36 P.K. Kennedy, *IEEE J. Quantum Electron.* **QE-31**, 2241 (1995)
- 37 E. Yablonovitch, N. Bloembergen, *Phys. Rev. Lett.* **29**, 907 (1972)
- 38 L.V. Keldysh, *Sov. Phys. JETP* **20**, 1307 (1965)
- 39 F. Williams, S.P. Varna, S. Hillenius, *J. Chem. Phys.* **64**, 1549 (1976)
- 40 A. Migus, Y. Gauduel, J.L. Martin, A. Antonetti, *Phys. Rev. Lett.* **58**, 1559 (1987)
- 41 A.M. Perelomov, V.S. Popov, M.V. Terent'ev, *Sov. Phys. JETP* **23**, 924 (1966)
- 42 K. Mishima, M. Hayashi, S.H. Lin, H.L. Selzle, E.W. Schlag, *Phys. Rev. A* **66**, 033401 (2002)
- 43 Q. Sun, H. Yang, Y. Liu, Z. Wu, H. Yang, Q. Gong, *Opt. Lett.* **30**, 320 (2005)
- 44 M. Nurhuda, E. van Groesen, *Phys. Rev. E* **71**, 066502 (2005)